SCIENCE CHINA
Technological Sciences

doi: 10.1007/s11431-012-4934-2

Three-dimensional aerodynamic optimization design of high-speed train nose based on GA-GRNN

YAO ShuanBao*, GUO DiLong & YANG GuoWei

Key Laboratory for Hydrodynamics and Ocean Engineering Institute of Mechanics, Chinese Academy of Sciences, Beijing 100190, China

Received January 13, 2012; accepted May 11, 2012

With the speed upgrade of the high-speed train, the aerodynamic drag becomes one of the key factors to restrain the train speed and energy saving. In order to reduce the aerodynamic drag of train head, a new parametric approach called local shape function (LSF) was adopted based on the free form surface deformation (FFD) method and a new efficient optimization method based on the response surface method (RSM) of GA-GRNN. The optimization results show that the parametric method can control the large deformation with a few design parameters, and can ensure the deformation zones smoothness and smooth transition of different deformation regions. With the same sample points for training, GA-GRNN performs better than GRNN to get the global optimal solution. As an example, the aerodynamic drag for a simplified shape with head + one carriage + tail train is reduced by 8.7%. The proposed optimization method is efficient for the engineering design of high-speed train.

aerodynamic drag, GA-GRNN, parametric, high-speed trains

Citation: Yao S B, Guo D L, Yang G W. Three-dimensional aerodynamic optimization design of high-speed train nose based on GA-GRNN. Sci China Tech Sci, 2012, doi: 10.1007/s11431-012-4934-2

1 Introduction

High-speed train is an important symbol of technology development. In recent years, high-speed train technology in China has achieved significant progress, and the train speed of the Beijing-Shanghai high-speed rail has reached 300 km/h. High-speed trains run close to the ground, and the aspect ratio is much larger than other ground vehicles. Thus, with the increasing running speed, the aerodynamic drag becomes much more complicated [1–3]. While the length of streamlined head is slightly longer than 5 m, the aerodynamic drag could take 85% of total resistance when the running speed is close to 300 km/h. This percentage changes to 75% when the length of the streamlined head reaches 10 m [4]. As a result, the aerodynamic drag reduction is very prominent and has become one of the key issues for aerodynamic shape optimization of high-speed trains. The head shape is a complex streamline which is controlled by dozens of design parameters. Currently, traditional methods, such as wind tunnel tests, dynamic model tests and real vehicle tests, are used to get the relationship between individual parameters and aerodynamic performance so as to perform aerodynamic shape design, which would take a long design cycle and cost a lot. With the development of computer technology, the computational fluid dynamics (CFD) technology is successfully used for high-speed train design. However, lots of operating conditions should be calculated in order to get a good aerodynamic design, which would require a great amount of computing resources, and the relationships between a single goal design parameter and optimization goals can only be obtained from those calculation results.

Few public works on high-speed train aerodynamic shape

*Corresponding author (email: ysbao566@163.com)

optimization design methods that combine CFD techniques with optimization algorithms can be found. The published research results mainly focused on two-dimensional model of train of longitudinal-type line or used inefficient optimization algorithms, which are difficult to apply to engineering problems that require large-scale computing resources and multi-parameters. Sun [5] proposed a method that combines genetic algorithms (GA) and arbitrary shape deformation (ASD) techniques. For few design parameters, it can reduce flow field computation, shorten the design cycle and find non-linear relationships between the optimization objectives and the design parameters. However, the CFD computation cost would geometrically increase with the number of design parameters, which is unbearable in engineering. In order to reduce the intensity of micro-pressure waves, optimization design of longitudinal-type line of high-speed trains has been studied in refs. [6–8]. An optimization algorithm that combines successive quadratic programming (SQP) optimization with support vector machine (SVM) which can be used for classification and nonlinear regression has been developed in ref. [6]. A certain number of sample points should be used for training the SVM to make it achieve required accuracy, then the optimal target is searched with SQP-based approximate optimization based on the trained model. It's extremely important for the training of SVM to select sensible sample points. A small number of training sample points is difficult to make SVM meet the required accuracy. Based on nine design variables, one hundred sample points were selected in ref. [6], which indicated that at least one hundred CFD analysis should be made in the optimization process. So the computation cost of this method is still too high. In this paper, a new parametric approach called local shape function (LSF) based on free-form surface deformation method has been designed for the optimization of streamlined shape of high-speed trains. In order to reduce aerodynamics drag of high-speed trains and saving computational time, five key design variables were extracted, sixteen sample points were designed by Sobol method, and the objective function that is used to find the smooth factors was devised with cross-validation method. The minimum response surface criterion was used to gradually increase the number of training sample points. After four times of adding points, the general regression neural network based on genetic algorithm (GA-GRNN) that can achieve the required engineering precision was designed. Combined with the real-coded genetic algorithm, a more efficient aerodynamic shape optimization method was designed, and an optimized simplified shape with head + one carriage + tail train based on CRH380A was found with the above approach. Then the simplified streamlined head was utilized in a real case, and a comparative study on aerodynamic performance of the optimal one and the prototype of CRH380A was performed.

2 General regression neural network based on genetic algorithm

GRNN that is constructed based on mathematical statistics is a type of radial basis function neural network (RBFNN). This approach does not require a pre-determined form of equations, instead, it uses the probability density function, so that it has a strong nonlinear mapping ability, flexible network structure, a high degree of error tolerance and robustness. Even if a small number of sample points exist, the output of the network can converge to the optimal regression surface, which is quite suitable for solving nonlinear problems. The value of spread of each neuron is the same in GRNN, and the training process of the network is a single-valued optimization process for the spread, which is not considered impact on output with different spreads, as a result, the prediction accuracy of the network is reduced. In order to improve the prediction accuracy of GRNN, the spread of each neuron is treated as an independent variable, and the best value of each spread is found by genetic algorithm depending on the degree of impact of output. Then a GA-GRNN model is constructed [9].

The theory of GRNN is based on non-linear regression analysis [9–12]. Assume that $f(\boldsymbol{x}, y)$ represents the probability density function of a random vector $\boldsymbol{x}$ and a random scalar variable y, with the value of $\boldsymbol{x}$ being $\boldsymbol{x}_0$. Then the conditional mean of y given $\boldsymbol{x}_0$ is given by

$$E(y / \boldsymbol{x}_0) = \hat{y}(\boldsymbol{x}_0) = \frac{\int_{-\infty}^{\infty} y f(\boldsymbol{x}_0, y)\mathrm{d}y}{\int_{-\infty}^{\infty} f(\boldsymbol{x}_0, y)\mathrm{d}y}. \tag{1}$$

Using a nonparametric estimate method proposed by Parzen, the density can be obtained by the following equation with a sample of observations $\{\boldsymbol{x}_i, y_i\}_{i=1}^{n}$.

$$f(x_0, y) = \frac{1}{n(2\pi)^{\frac{p+1}{2}}\sigma_i^{p+1}} \sum_{i=1}^{n} \mathrm{e}^{-d(\boldsymbol{x}_0, \boldsymbol{x}_i)} \mathrm{e}^{-d(y, y_i)}, \tag{2}$$

where $d(\boldsymbol{x}_0, \boldsymbol{x}_i) = \sum_{j=1}^{p} [(x_{0j} - x_{ij}) / \sigma_i]^2$, $d(y, y_i) = [y - y_i]^2$, n is the number of sample observations, p is the dimension of the vector variable $\boldsymbol{x}$ and σ_i is the width for Gaussian function of each neuron. If all of the values of σ_i are the same, the neural network is GRNN, otherwise, GA-GRNN.

Combining eqs. (1) and (2), and interchanging the order of integration and summation, we will result in the designated equation, which takes the form as below:

$$\hat{y}(\boldsymbol{x}_0) = \frac{\sum_{i=1}^{n} \left(\mathrm{e}^{-d(\boldsymbol{x}_0, \boldsymbol{x}_i)} \int_{-\infty}^{+\infty} y \mathrm{e}^{-d(y, y_i)} \mathrm{d}y \right)}{\sum_{i=1}^{n} \left(\mathrm{e}^{-d(\boldsymbol{x}_0, \boldsymbol{x}_i)} \int_{-\infty}^{+\infty} \mathrm{e}^{-d(y, y_i)} \mathrm{d}y \right)}. \tag{3}$$

Since $\int_{-\infty}^{+\infty} z\mathrm{e}^{-z^2}\mathrm{d}z = 0$, eq. (4) will be obtained by performing the indicated integrations:

$$\hat{y}(\boldsymbol{x}_0) = \frac{\sum_{i=1}^{n} y_i \mathrm{e}^{-d(\boldsymbol{x}_0, \boldsymbol{x}_i)}}{\sum_{i=1}^{n} \mathrm{e}^{-d(\boldsymbol{x}_0, \boldsymbol{x}_i)}}. \quad (4)$$

So $\hat{y}(\boldsymbol{x}_0)$ is the weighted value of the dependent variables' values of all training samples, and the weight factor is $\mathrm{e}^{-d(\boldsymbol{x}_0, \boldsymbol{x}_i)}$.

Figure 1 shows the overall block diagram of GA-GRNN that is composed of the input layer, the pattern layer, the summation layer and the output layer. The elements in the input layer are simply the linear elements, which provide all of the measurement variables to all of the neurons in the pattern layer, and each training sample point has a unique element. In the pattern layer, every neuron has an activation function that usually is Gaussian function $\mathrm{e}^{-d(\boldsymbol{x}_0, \boldsymbol{x}_i)}$. When a new vector $\boldsymbol{x}$ is entered into the network, it is subtracted from the stored vector representing each cluster center. Either the squares or the absolute values of the differences are summed and fed into the activation function. The summation layer performs the dot product between a vector composed of the signals from the pattern layer. It has two neurons: One is called numerator neuron that is used to generate a summation of the outputs of the pattern layer weighted by the number of observations each cluster center represents; the other is called denominator neuron that is used to generate a summation of the outputs of the pattern layer. The output layer merely divides the value of denominator neuron by the value of numerator neuron to yield the desired estimate of *y*.

3 Local shape function parametric approach

3.1 Geometry

Optimal head design of high-speed trains mainly focuses on the streamlined parts, of which the key design parameters are: the cross-sectional area distribution of the nose of the high-speed trains, the slenderness ratio of streamlined head, the longitudinal-type line and horizontal-type line of the streamlined head, nose drainage, cab perspective and the side hood of bogie. The model used for shape optimization is a simplified prototype of CRH380A, which consists of a leading car, a middle car and a rear car. The shield is completely closed and the cavity around the bogie zone is closed too, so that the aerodynamic drag caused by the bogie zone is not considered in the present model.

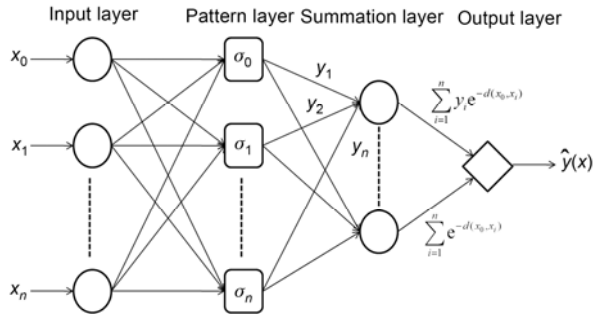

Figure 1 GA-GRNN block diagram.

The geometric parameters of the simplified shape of CRH380A are as follows. The length of each carriage is 25 m, and the shape of the rear car is the same as the leading car. The length of the streamlined head is 12 m, the height is 3.5 m, the width is 3.38 m, the cross-sectional area is 11.2 m^2 and the slenderness ratio is 3.55. The type of the cross sectional area distribution of CRH380A is a three-sectional type, of which the longitudinal-type line is double-arch, the horizontal-type line is flat spindle and the nose is ellipsoid, as shown in Figure 2.

3.2 Local shape function parametric approach

Geometry parametric approach plays an important role in aerodynamic optimization design. An efficient parametric method can not only describe the changes of shape completely, but also reduce the optimization cycle and improve optimization efficiency. The popular surface parametric methods are as follows: the free form surface deformation (FFD) method, the NURBS method and the grid method. Although the grid method can describe an arbitrary shape, it may generate non-streamlined surface, and lead to irrational flow. The performance of FFD method [13] and NURBS method are perfect, which can control large deformation regions with a few control points and ensure the smoothness of surface. In this paper, a new parametric approach called local shape function (LSF) which is based on FFD method and NURBS method was designed.

Implementation steps are as follows.

1) For a given geometry, deformation regions should be divided firstly.

2) Mesh the deformation regions, and obtain the coordinate value of every grid point.

3) Choose the deformation function of each region, which can be selected at random, but smooth transition between adjacent regions should be considered.

4) Choose a weight factor W_i for each deformation function, which determines the maximum deformation value of each region.

5) Calculate the increments Δ of coordinates of all grid points by the deformation functions and W_i.

6) Get the coordinates of the deformed shape by summing Δ and the coordinates of the original shape.

7) According to the coordinates of the deformed shape, the deformation surface can be fitted exactly, then a defor-

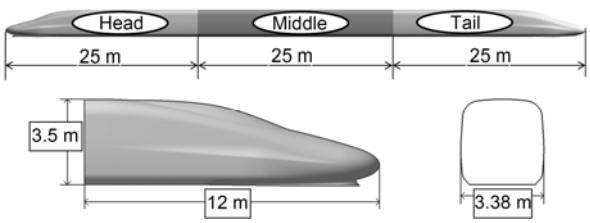

Figure 2 The geometric parameters of the simplified shape of CRH380A.

mation process is done.

In the process, step 3) is the most key step. The deformation surfaces are different from each other due to the choice of deformation functions. Inappropriate deformation functions will easily lead to irrational deformation surfaces. Trigonometric functions, exponential functions, logarithmic functions, polynomial functions and NURBS functions are all commonly used deformation functions.

Due to the symmetrical design along the longitudinal of the train, only one side of the symmetrical plane of the streamline is parameterized. As a result, the design parameters can be reduced by half. The parametric surfaces are separated into five deformation regions, as shown in Figure 3. Nose drainage is controlled by nose deformation region; a control point Point1 is chosen, and two design parameters are extracted, which are W_1 and W_2 that control the length and height of the nose, respectively. The width of the streamline is controlled by the transition zone, the bottom side and the cab zone, and the coordinate W_3 of the control point Point2 along the width direction is extracted to be the third design parameter. The coordinate W_4 of the control point Point3 on the cab region along the height direction of the streamline is extracted as the fourth design parameter to control the cab view. The coordinate W_5 of the control point Point4 on the cowcatcher along the length direction of the streamline is extracted as the fifth design parameter to control the cowcatcher shape. For simplicity, all the deformation functions in this paper are trigonometric functions. Figure 4 shows the deformation of the nose cone and the cowcatcher. As seen below, the deformation method can ensure the surface smoothness and smooth transition among different deformation regions.

4 Numerical approach and validation

4.1 CFD method

CFD accuracy that directly affects the construction of the response surface function and efficiency of optimization algorithm is the basis for the whole optimization process. In this paper, the speed of high-speed train was 300 km/h, so the Mach number was 0.245. In this condition, the air compression characteristic had an obvious effect on the aerodynamic drag of the train. Therefore, the steady compressible

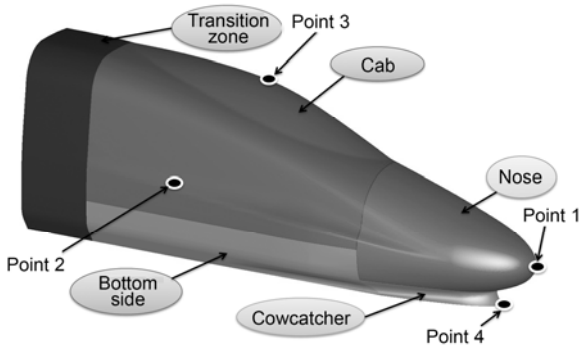

Figure 3 Control points and deformation regions of nose.

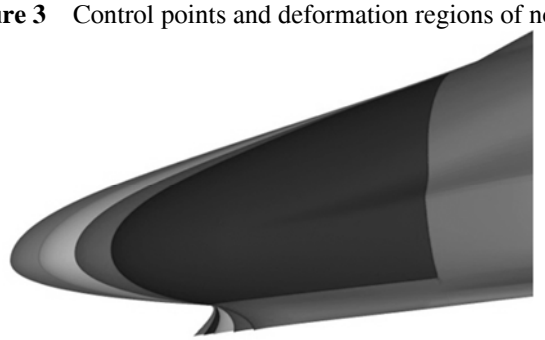

Figure 4 The deformation of nose cone and cowcatcher.

Reynolds-averaged Navier-Stokes eq. [14] that are based on the finite volume method were used to predict the aerodynamic drag. Roe's FDS scheme was used to calculate convective fluxes, and lower-upper symmetric Gauss-Seidel (LU-SGS) was chosen for temporal discretisation. The *k-ω SST* model [15] was selected as the turbulence model. The standard wall functions were used near the wall so that the accuracy of the CFD results could be ensured with a limited amount of mesh.

Computational domains and boundary conditions: with the length of the simplified train being the characteristic length L, the length of inflow direction is $1L$, the length of outflow direction is $2L$, the width is $2L$ and the height is $1L$, as shown in Figure 5. The flow velocity is 83.33 m/s; the far-field pressure is 1 atm, the temperature is 288 K and the reference area is the maximum cross-sectional area of the train. As a result of the compressibility calculation model, one dimensional inviscid flow of the Riemann invariants were introduced as the far-field boundary conditions, which are also known as non-reflective boundary conditions. Inflow, outflow and the top boundaries were all set as far-field boundary conditions and the train body was non-slip solid wall boundary condition. The ground was treated as the moving wall so as to simulate the ground effect, and the moving speed was equal to the train speed.

4.2 Grid-independent verification

Mesh quality has a direct impact on the accuracy and

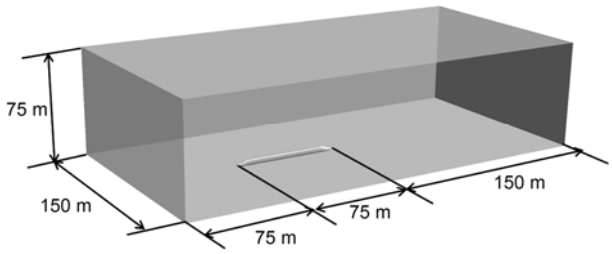

Figure 5 The computational domain.

stability of the calculation results. Thus, grid-independent verification was done with different amounts of spatial meshes that combine prism mesh near the wall and hexahedral meshes so as to assess the influences of different spatial meshes on the calculation results. With the thickness of the first prism layer meeting the requirement of the wall function, four sets of mesh were used in this paper, and the amounts of the grids were 8.4 million, 10.3 million, 12.7 million and 44.9 million, respectively. The distribution of spatial grids is shown as Figure 6.

Figure 7 shows that different numbers of meshes have almost no effect on the calculation results. The drag coefficient variation of different compartments is very small, and the variation of total drag coefficient is less than 1%. Besides, the fluctuation of pressure drag and frictional drag is also very small. So the influence of method of spatial grid division on the calculation result can be ignored. Thus, the set of 8.4 million grids was chosen in order to improve the efficiency of optimal process.

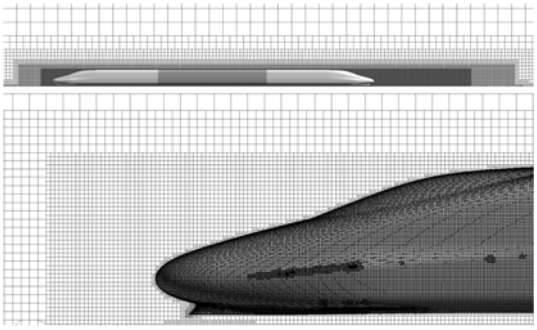

Figure 6 The distribution of grids.

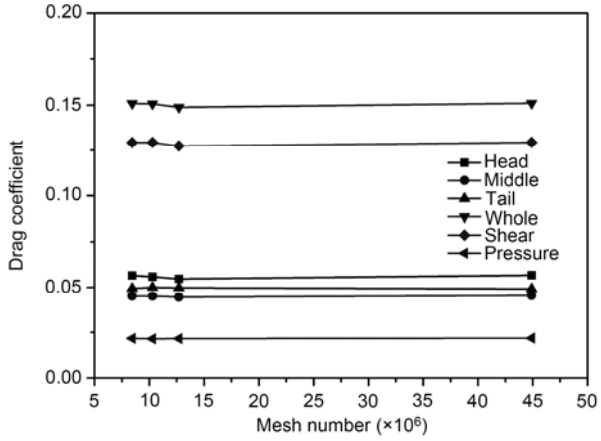

Figure 7 Calculation results with different numbers of meshes.

5 The construction and precision analysis of GA-GRNN

5.1 Sampling method and selection of sample points

In this paper, the total aerodynamic drag coefficient of simplified shape of CRH380A was treated as the optimization target. Given the appropriate constraints, the optimal design parameters which result in the minimum value of the total aerodynamic drag coefficient would be found with GA-GRNN. In order to facilitate parameterization of the streamline, the real geometry was united along the length of the nose, so that the length of the streamline was 1 m. After the aerodynamic drag of the train was numerically obtained, the united geometry was enlarged to the real shape so as to eliminating the influence of the united shape on the calculation result. The bound ranges of the five design parameters (unit is mm) were as follows: length of the nose: $0 \leqslant W_1 \leqslant 83.333$, height of the nose: $-15 \leqslant W_2 \leqslant 10$, width of the body: $-30 \leqslant W_3 \leqslant 0$, the cab angle: $-10 \leqslant W_4 \leqslant 4$, shape of the cowcatcher: $-60 \leqslant W_5 \leqslant 10$. Considering the influence of the length of nose cone and the width of train body on aerodynamic drag into consideration, the nose length of initial shape was set to be the minimum boundary of the nose length and the body width of initial shape was set to be the maximum boundary of the body width. The selection of sample points is crucial to catch the relationship between design space and the optimization target. As a pseudo-random algorithm, Sobol sampling method [16] can make the distribution of initial sample points more uniform in the design space compared to the random sampling method. Thus, the Sobol method was used in the present paper as the sampling method. The number of the initial sample points was 16. 14 points were selected as the training points, and the other two points were the test points, as shown in Table 1. As seen in Table 1, *Cd* of design points are better than that of initial shape, which primarily reflects the better selection of the design space. Finding the best solution in a design space where more optimal solutions can not only reduce the number of sample points, but also be conducive to construct more accurate response surface models with the same number of sample points and get the global optimal solution more efficiently.

5.2 Validation of the efficiency of genetic algorithm

The training process of GA-GRNN is a multi-parameter optimization process to find the best value of the spread factors σ_i of each neuron based on the real-coded genetic

Table 1 Training points and test points

Type of sample points		W_1 (mm)	W_2 (mm)	W_3 (mm)	W_4 (mm)	W_5 (mm)	Cd
Training points	1	0.000	0.000	0.000	0.000	0.000	0.15091
	2	−41.667	−2.500	−15.000	−3.000	−25.000	0.14411
	3	−62.500	−8.750	−22.500	−6.500	−42.500	0.14034
	4	−20.833	3.750	−7.500	0.500	−7.500	0.14822
	5	−52.083	0.625	−18.750	−4.750	−33.750	0.14265
	6	−10.417	−11.875	−3.750	2.250	1.250	0.14797
	7	−72.916	6.875	−26.250	−8.250	−51.250	0.13992
	8	−31.250	−5.625	−11.250	−1.250	−16.250	0.14533
	9	−57.291	8.438	−1.875	−2.125	−3.125	0.15014
	10	−15.625	−4.063	−16.875	−9.125	−38.125	0.14241
	11	−78.125	2.188	−9.375	1.375	−20.625	0.14638
	12	−36.458	−10.313	−24.375	−5.625	−55.625	0.13923
	13	−67.708	−7.188	−13.125	3.125	−11.875	0.14505
	14	−26.042	5.313	−28.125	−3.875	−46.875	0.13965
Test points	15	−46.875	−13.438	−5.625	−0.375	5.625	0.14675
	16	−5.208	−0.938	−20.625	−7.375	−29.375	0.14202

optimization algorithm. In order to verify global optimization capability of the genetic algorithm used in this paper, Shaffer's F_2 function was chosen to be the test function, whose expression is

$$F_2 = 0.5 - \frac{\sin^2\sqrt{x_1^2 + x_2^2} - 0.5}{(1 + 0.001(x_1^2 + x_2^2))^2},$$
$$-10.0 < x_1 < 10.0, -10.0 < x_2 < 10.0.$$

This function has an infinite number of local maxima, and the global maximum $F_2(x_1, x_2)$=1.0 appears only at (x_1, x_2)=(0.0, 0.0). As parameters for GA operation, the size of initial population was set to 150. The probabilities of crossover and mutation were set to 0.6 and 0.3, respectively. The size of evolution generation was set to 100. The fitness function is expressed as f=1/$F_2(x_1, x_2)$.

The optimal value was $F_2(x_1, x_2)$=1.0000 at $(x_1^*, x_2^*) = (0.0001, 0.005)$. As shown in Figure 8, the average fitness value can quickly converge to the global optimal solution, which means that the GA used in this paper had a strong capability to get the global optimization result.

5.3 Construction of GA-GRNN and precision analysis

As the number of initial training points was only 14, the genetic algorithm and cross-validation method were used for training the neural network in order to make full use of information of each sample point. For the initial 14 sample points, we took each point as a group, selected 13 groups from the 14 groups as the training set, and took the rest one as the verification sample point, so that each sample point was treated as the verification sample point for one and only one chance. The average relative error of all verification points was taken as the objective function for genetic algorithm optimization.

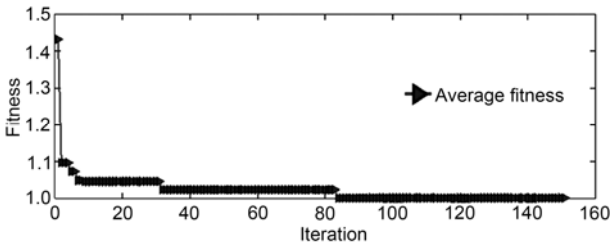

Figure 8 History of average fitness value of test function along with the evolution number.

For GRNN, values of all of the spread factors are the same, so it is a single-valued optimization process to get the best value. But for GA-GRNN, each training sample point has a unique neuron, so 13 neurons are needed for GA-GRNN construction with 13 training sample points, and 13 spread factors $\sigma_i (i = 1, \cdots, 13)$ are needed for optimization. A suitable GA-GRNN model cannot be constructed only with the initial 14 sample points, thus, the minimizing response surface method [17] was used to improve the prediction accuracy of the model. The guideline for adding sample points was to take the best point found based on the initial response surface model into the training set so that the prediction accuracy around the optimal solution region increases gradually.

The genetic algorithm parameters for GRNN to get the best spread value were as follows: The size of initial population was set to 60, the probabilities of crossover and mutation were set to 0.9 and 0.2, respectively, the size of evolution generation was set to 650. The genetic algorithm parameters for GRNN to get the optimal value were as follows: The size of initial population was set to 50, the probabilities of crossover and mutation were set to 0.9 and 0.5, respec-

tively. The size of evolution generation was set to 2500.

The genetic algorithm parameters for GA-GRNN to get the best spread value were as follows: The size of initial population was set to 60, the probabilities of crossover and mutation were set to 0.95 and 0.3, respectively, the size of evolution generation was set to 500. The genetic algorithm parameters for GRNN to get the optimal value were as follows: The size of initial population was set to 40, the probabilities of crossover and mutation were set to 0.9 and 0.2, respectively. The size of evolution generation was set to 500.

Figure 9 shows the prediction errors of GRNN and GA-GRNN changing with the number of iterations. As seen below, with the increasing number of training sample points, the prediction accuracy of the two models increased gradually in the optimal solution region. For GRNN, the prediction accuracy in other design regions was essentially the same, but for GA-GRNN, the value increased slightly. GRNN prediction accuracy was still greater than 1% after adding 12 points, while GA-GRNN prediction accuracy reduced to less than 1% only for two points. Thus, GA-GRNN can be a better mapping model between design parameters and optimization target. Therefore, GA-GRNN model was utilized to find the optimal solution.

5.4 Optimization process

Figure 10 shows the overall optimization design process. Firstly, Sobol sampling method was used to obtain the initial sample points, the accurate objective value of which was calculated by CFD simulation. Then a certain number of initial sample points for training GA-GRNN model were selected by the genetic algorithm. When the predication accuracy of the RSM met the engineering requirement, GA was called again to search the optimization values of design parameters. If the optimal solution was worse than the target value, the sample point of worst performance among the training points would be replaced by the optimal solution, so that the prediction accuracy of GA-GRNN continuoued to be improved with the same overall number of training samples; otherwise, the final RSM was built up. CFD analyses is the basis of the optimization process, the construction and prediction accuracy of GA-GRNN is the core of the process, and the number of sample points that are used to train the GA-GRNN is directly related to the optimize efficiency. Thus, using as less training points as possible to construct as more accurate prediction results of GA-GRNN as possible was focused in this work. It can be observed that the real-coded genetic algorithm played an important role in the optimization process which was adopted almost in each step of the optimization process.

6 Results and discussion

6.1 Comparative analysis between original shape and optimal shape

The total aerodynamic drag coefficient C_d of the simplified CRH380A model was treated as the optimization objective and the fitness function was taken as $f=C_d$. The initial population was set as n_p=50. The roulette method was used as the selection operator, while the probabilities of crossover and mutation were set to 0.9 and 0.5, respectively, and the size of evolution generation was set to 80. Figure 11 shows the history of average fitness value of the test function along with the evolution number, showing that the average fitness value converged to a stable value quickly.

Table 2 shows the CFD results and predicted values of the GA-GRNN model. The prediction error was only 0.38%, indicating that the response surface model is feasible.

The simplified CRH380A model did not include the subsidiary parts such as the bogies, windshields and pantoraphs. As a result, the inviscid drag of the train was less than the viscous drag. Table 3 shows the viscous drag of the optimal shape was almost unchanged compared to the orig-

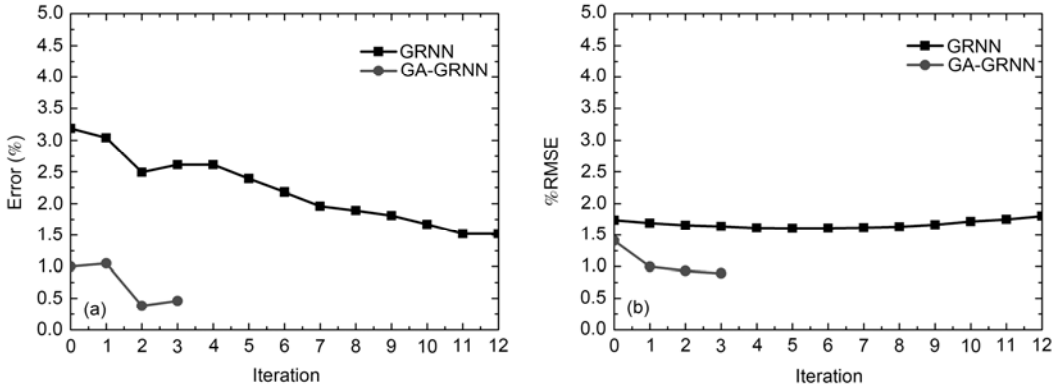

Figure 9 (a) The relative error between the true values and predicted values of GRNN and GA-GRNN; (b) the RMSE of test sample points for the true values and the predicted values of GRNN and GA-GRNN ($\%\mathrm{RMSE}=100\sqrt{\frac{1}{n_s}\sum_{i=1}^{n_s}(y_i-y_i^{(p)})^2}\Big/\frac{1}{n_s}\sum_{i=1}^{n_s}y_i$, where n_s is the number of test sample points, y_i is actual value, and $y_i^{(p)}$ is the predictive value).

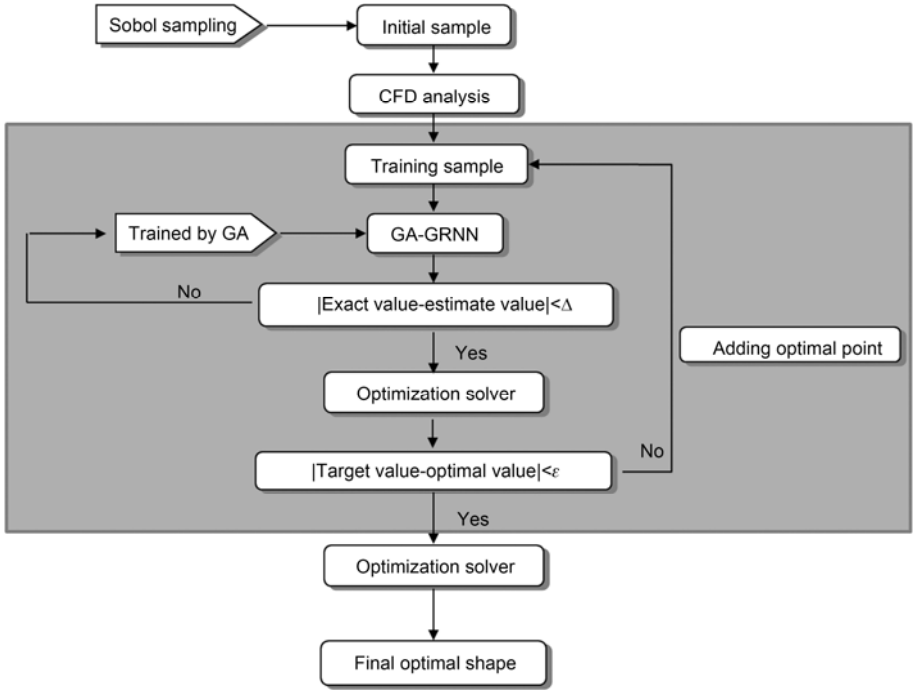

Figure 10 The optimization design process of high-speed train head.

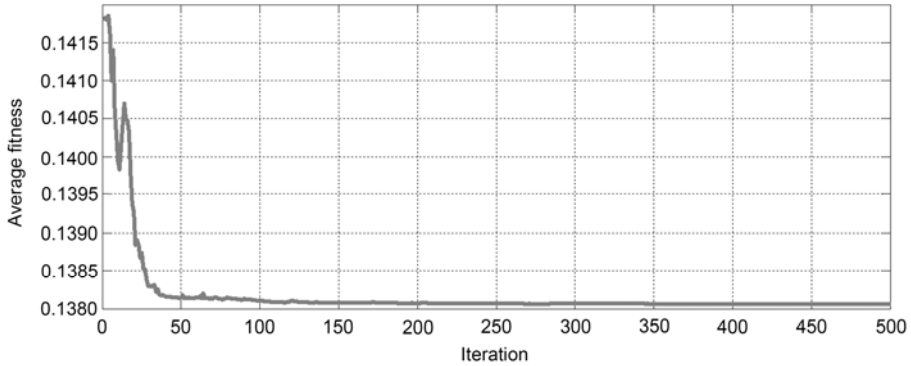

Figure 11 History of average fitness value of test function along with the evolution number.

Table 2 Comparison of the CFD result and GA-GRNN performance of the optimization

Actual value	GA-GRNN	Prediction error
0.13778	0.13831	0.38%

inal shape, but the inviscid drag reduction were 53.28%. The drag coefficient of the middle car changed little, while the drag reduction of the head and tail were almost the same, which were certainly due to the reduction of inviscid drag. Results revealed that the inviscid drag was more sensitive to the change of the streamline, which becomes the main objective of aerodynamic drag reduction of high speed trains.

After optimization, the length of the streamline increased about 0.436 m; the height of the nose reduced about 0.178 m; the largest reduction of width of the streamline was about 0.715 m; the inclination of the glass on the cab reduced about 0.95° and the vertex location of the cowcatcher bottom moved back about 0.716 m, as shown in Figure 12.

The viscous drag coefficients of the original head car and tail car were 0.04593 and 0.03851, while the inviscid drag coefficients were 0.01061 and 0.01088, respectively. However, the viscous drag coefficients of the optimal head car and tail car were 0.04503 and 0.0375, while the inviscid drag coefficients were 0.00424 and 0.00567, respectively. So the viscid drag changed little after optimization, while the inviscid drags of head car and tail car were reduced by 60.03% and 47.89%, respectively. Figure 13 shows the surface pressure distribution, the longitudinal velocity distribution of original shape and optimal shape, and the speed distribution along the train central axis. Compared to the original shape, the development of the boundary layer at the top of the optimal shape is essentially the same, but the flow field around the nose and tail are significantly different. As the nose gets sharpened, the high pressure zone around the nose is reduced, and the decrease of cab inclination leads to a smooth variation of the air flow around the transition zone.

As the tail cone gets sharper and longer, the separation of the wake is delayed, and the turbulence strength of the trail flow field becomes weaker, which decreases the pressure gradient along the streamline. As a result, the inviscid drag on the leading car and trailing car reduces a lot.

After optimization, the cowcatcher changed from the forward type to the backward type. The small eddy Vc1 disappeared in the optimal model and only Vc2 existed below the cowcatcher. However, the strength of Vc2 had been greatly weakened, as shown in Figure 14. The smooth transition between the cowcatcher and the bottom of the body reduced the disturbance of the flow field here, so the air speed-up process became more stable, leading to the reduction of the high-pressure zone around the cowcatcher. As a result, the inviscid drag of the streamline was reduced, too.

Figure 15 shows the change of vortex cores in the wake zone of original shape and optimal shape. Two steady vortices Vc1 and Vc2 were developed along the surface of the streamline of the trailing car, and two more intense steady vortex Vc3 and Vc4 were detached on the cowcatcher. The intense of these eddies determined the strength of negative pressure around trailing streamline. After optimization, the strengths of the four vortexes Vc1, Vc2, Vc3 and Vc4 were significantly reduced, resulting in weaker strength of negative pressure in the wake region, thus, the inviscid drag was also reduced.

Figure 16 shows the *Cp* distribution along the longitudinal-type line of the original shape and optimal shape. Compared to the original shape, the *Cp* distribution of the optimal shape along the middle surface of the train changed little. However, the *Cp* around the cowcatcher of the leading car and the trailing car changed a lot. The positive *Cp* of head cowcatcher reduced, and the negative *Cp* of tail cowcatcher also reduced, which obviously reduced the inviscid drag of the optimal shape.

If the maximum cross-section area of the train is constant, the cross-section area distribution of the streamline has a direct impact not only on interior volume distribution of the nose and cab, but also on the flow field around the nose. Figure 17 shows the cross-section area distribution of original shape and optimal shape, in which *L* is the length of streamline and Aref is the maximum cross-sectional area of CRH380A. Compared to the original shape, the cross-sectional area of the optimal streamline reduces a lot, which reduces the frontal area of the nose, so the high pressure region around the head reduces, too. The cross-sectional area distribution of the optimal shape is more smooth around the nose and cab, which makes the air acceleration process more stable in front of the nose and reduces the strength of the flow disturbance. The distribution becomes more severe on the region that connects the streamline and the straight part, which makes the air speed-up more quickly in the transition zone, and leads to a large low-pressure region there. As a result, the inviscid drag of the head decreases a lot.

Table 3 Comparison of the CFD result and GA-GRNN performance of the optimization

	Total	Viscid	Inviscid	Head	Middle	Tail
Original shape	0.15091	0.12937	0.02154	0.05654	0.04498	0.04939
Optimal shape	0.13778	0.12784	0.00994	0.04927	0.04534	0.04317
Drag reduction	8.7%	1.18%	53.28%	12.86%	−0.8%	12.59%

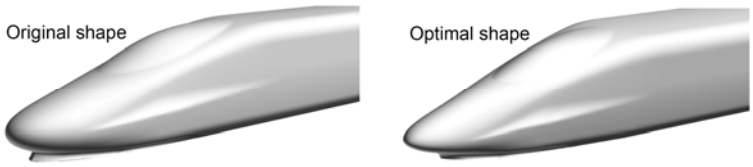

Figure 12 The original shape and optimal shape of CRH380A.

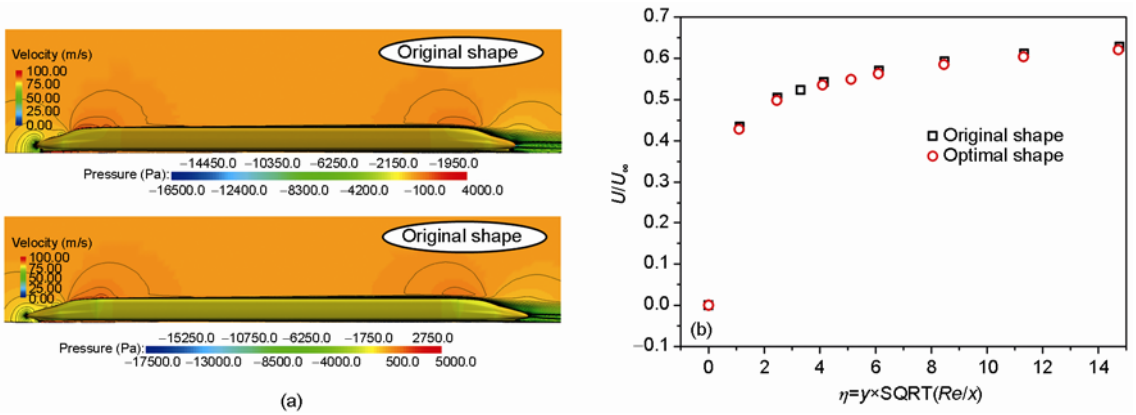

Figure 13 (a) The surface pressure and the longitudinal velocity contours of the original shape and optimal shape; (b) the speed distribution along the train central axis.

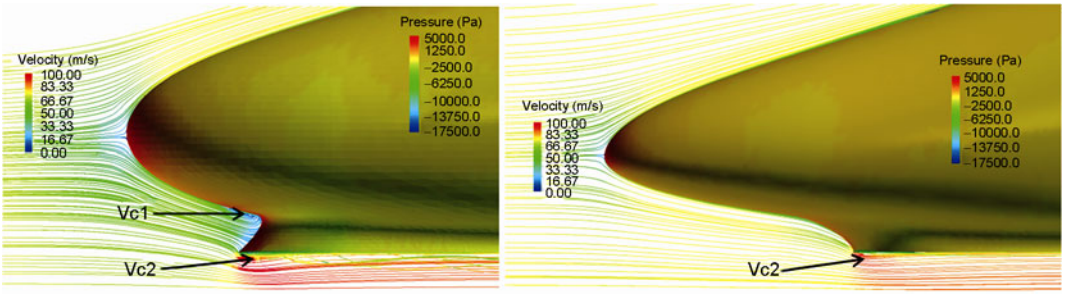

Figure 14 The surface pressure contours and streamlines along the original shape and optimal shape.

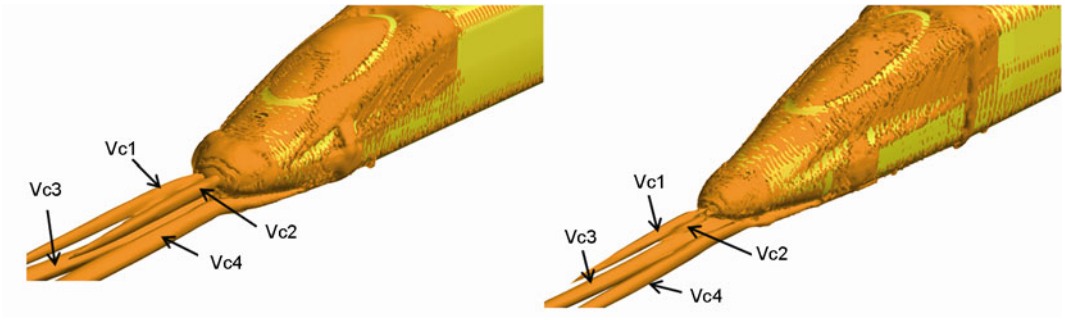

Figure 15 Transient Q isosurface graphs around the wake of original shape and optimal shape (Q=100).

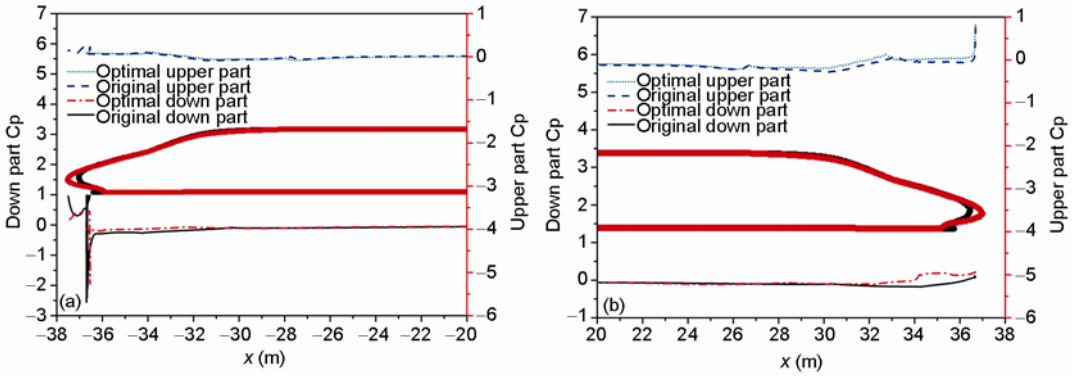

Figure 16 The *Cp* distribution of the longitudinal-type line of the original shape and optimal shape. (a) The *Cp* distribution of the longitudinal-type line of train head; (b) the *Cp* distribution of the longitudinal-type line of train tail.

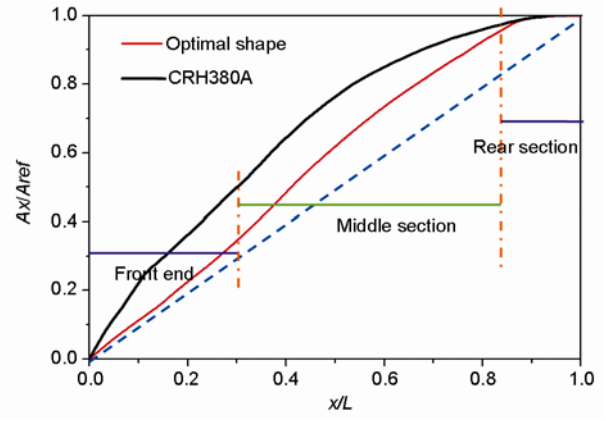

Figure 17 The cross-section area distributions of original shape and optimal shape.

6.2 Comparative analysis of real original shape and real optimal shape

Since only the streamline is considered to be optimized, in order to reduce time that is taken for grid generation and the flow field calculation, the real shape of CRH380A (with the real windshields and bogies included) was simplified, and the ancillary components were discarded. However, the subsidiary parts have a great influence on the aerodynamic drag of the real shape [2]. Thus, the aerodynamic performances of the true shape of the prototype vehicle and optimal vehicle would be analyzed in the next section in order to study the drag reduction efficiency of optimal shape.

In order to make a comparative study with experimental data, the calculation conditions were set to be the same as

the wind tunnel test conditions. The computational model was the 1:8 scale model so as to be the same as the experimental model. The pressure-coupled equations of semi-implicit method (SIMPLE) were used for calculating the flow field, the turbulence model was SST *k-w*, and the standard wall function was used near the wall. The flow speed was 60 m/s, the ground was the stationary wall, velocity inlet boundary condition and pressure outlet boundary condition were used at the inlet and outlet, respectively. Slip wall condition was used in the far-field. The types of space meshes were composed of polyhedrons and the prism boundary layer mesh near the train surface. The total number of the volume meshes was about 28.4 million, and the mesh in specific locations is shown in Figure 18.

The inviscid drag of the real vehicle was slightly larger than the friction drag, as shown in Table 4. Compared to the total aerodynamic drag of the wind tunnel test, the error of the numerical results was less than 1%, indicating that the calculation results were reliable. After optimization, the total *Cd* of 380A reduced about 8.86%, the viscous drag was almost unchanged, but the inviscid drag reduced a lot. So the drag reduction efficiency kept the same as the simplified shape. Besides, the aerodynamic drags of the leading car, the middle car and the trailing car of the optimal middle were all smaller than those of original shape. However, the drag reduction efficiency of different sections of the real shape was different from that of the simplified shape, especially the middle car, the drag of which was almost constant for the simplified shape but reduced about 12.55% for the real shape.

Figure 19 shows the aerodynamic drag distribution of the components of the real shape. The *Cd* of the first bogie was obviously larger than those of the others, which was mainly because the air had been compressed for the second time

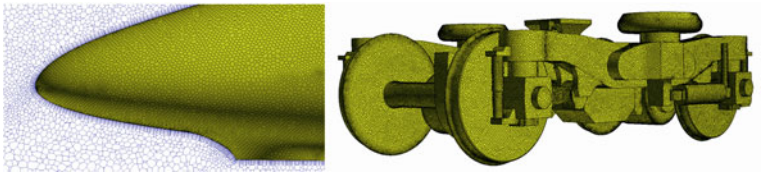

Figure 18 Local mesh of the real vehicle.

Table 4 The Cds and the drag reduction percentages of the real original and optimal vehicles

	Total	Viscid	Inviscid	Head	Middle	Tail
Wind tunnel test	0.32612	–	–	–	–	–
Original shape	0.32822	0.15088	0.17734	0.11519	0.0889	0.12413
Error	0.64%	–	–	–	–	–
Optimized shape	0.29914	0.14836	0.15078	0.10965	0.07774	0.11175
Drag reduction	8.86%	1.67%	14.98%	4.81%	12.55%	9.97%

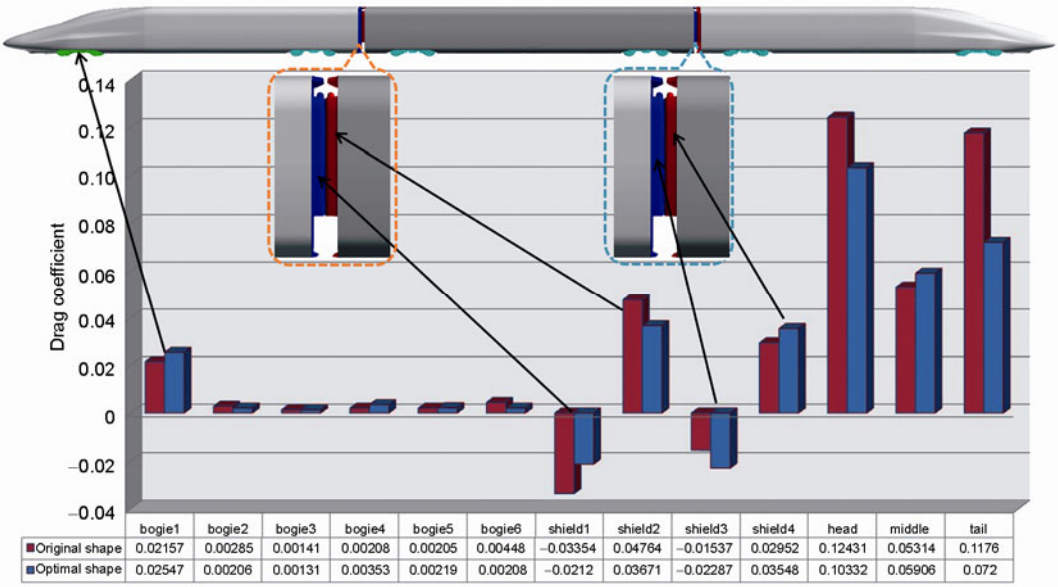

Figure 19 *Cds* of different components of the real shape.

near the cowcatcher and then flowed into the first bogie cavity at a higher speed, which generated a high pressure and led to the pressure drag of the first bogie larger than that of the others. The connection parts were divided into four parts so as to study the influences of the wind-shield on different sections conveniently. The four parts were named shield1, shield2, shield3 and shield4, as shown in Figure 14. The *Cds* of shield1 and shield3 were negative, meaning that the aerodynamic forces of the two parts are a kind of thrusting force. Conversely, the aerodynamic forces of shield2 and shield4 were a kind of resistance force. Shield2 and shield3 were the subsidiary parts of the middle section. Before optimization, the algebra summation of the aerodynamic forces of shield2 and shield3 was 0.03227. However, after optimization, the value changed to 0.01384, while the aerodynamic drags of other parts of the middle section changed little. As a result, the aerodynamic drag of the middle section of the optimal shape was smaller than that of the original shape. Except for the ancillary parts, the aerodynamic drags of the leading car and middle car reduced a lot. So the subsidiary parts of the train had a great impact on the distribution of the train aerodynamic drag. As a result, the simplified shape can reflect the true shape on the drag reduction and can significantly improve the optimization efficiency. Therefore, the appropriate simplified shape can be applied to high-speed train aerodynamic shape optimization.

6.3 The influence of design parameters on the aerodynamic drag of CRH380A

Reasonable design parameters have a direct impact on the final optimal results. Figure 20 shows the impact of design parameters on the drag coefficient gradient of the high-speed train. It can be observed that W_1 which controls the length of the nose has a minimal impact on the objective function gradient. Since the slenderness ratio of the original shape is 3.55, a greater value has little effect on the aerodynamic drag reduction. Therefore, the slenderness ratio cannot be blindly increased to reduce the aerodynamic drag. All the other four design parameters have a great influence on the objective function gradient. W_3 that controls the width of streamline has the greatest impact on the drag coefficient gradient. Thus, the cross-sectional area distribution is essential to high-speed train aerodynamic drag reduction. W_5 controls the cowcatcher shape, and also has a great impact on aerodynamic drag gradient. At present, cowcatchers used on high-speed train in China and other countries are all designed to be forward. However, the optimization results show that the backward-type cowcatcher is more favorable for aerodynamic drag reduction. Thus, backward-type cowcatchers are recommended to be used on high-speed train to improve the aerodynamic performance.

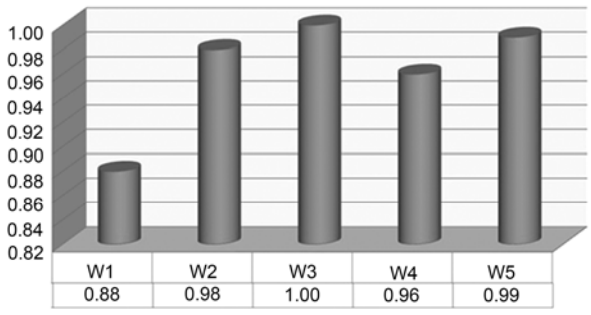

Figure 20 Impact factors of design parameters on the gradient of objective function.

All of the design parameters extracted in this work have an impact on the gradient of the objective function values and can fully describe the key features of the streamline on the condition of ensuring the basic characteristics of the original shape. That indicates that the selected design parameters are reasonable, and the corresponding parametric methods can be well applied to the high-speed train head design optimization.

7 Conclusions

In this paper, focusing on the simplified CRH380A model, five design parameters were extracted, the aerodynamic optimization of the streamline aiming at reducing the drag has been done with the conclusions as follows.

1) The local shape function (LSF) parameterization method that can control a large deformation zone with a few design parameters is simple yet practical, and this method can ensure the smoothness of the deformation zones and the smooth transition of different deformation regions. Thus, LSF can be well adopted for high-speed train aerodynamic shape optimization.

2) Using the same sample points for training, the prediction accuracy of GA-GRNN is obviously better than that of GRNN. Thus, the global optimal solution can be found more easily with GA-GRNN. Therefore, GA-GRNN model is recommended for global optimization.

3) After optimization, the total aerodynamic drag of simplified CRH380A model is reduced by 8.7%, the viscous drag reduces about 1.18% and the inviscid drag reduces about 53.85%. So inviscid drag is more sensitive to the deformation of aerodynamic shape and is the main target for drag reduction. Aerodynamic drag reduction of the head section is 12.86% and the value of the tail section is 12.59%. The results show that the aerodynamic shape optimization method proposed in this paper is simple yet efficient, and can be well used in high-speed train aerodynamic shape optimization .

4) The ancillary components have a great impact on the aerodynamic drag of trains, especially the connection parts, which seriously affect the distribution of aerodynamic drag. However, the simplified model still can be used as a substitute for the prototype model to perform the study on drag

reduction and thus can significantly improve the optimization efficiency. Therefore, the appropriately simplified model can be applied to high-speed train aerodynamic shape optimization.

This work was supported by the National Basic Research Program of China ("973" Project) (Grant No. 2011CB711100), the National Hi-Tech Research and Development Program of China ("863" Project) (Grant No. 2009BAQG12A03), and Computing Facility for Computational Mechanics, Institute of Mechanics, Chinese Academy of Sciences was gratefully acknowledged.

1 Raghuathan S，Kim H D，Setoguchi T. Aerodynamics of high-speed railway train. Prog Aerosp Sci, 2002, 8: 469–514
2 Baker C. The flow around high speed trains. J Wind Eng Industr Aerodynam, 2010, 98: 277–298
3 Tian H Q. Formation mechanism of aerodynamic drag of high-speed train and some reduction measures. J Cent South Univ Technol, 2009, 16: 0166–0171
4 Tian H Q. Train Aerodynamics. Beijing: China Railway Publishing House, 2007. 160–161
5 Sun Z X, Song J J, An Y R. Optimization of the head shape of the CRH3 high speed train. Sci China Tech Sci, 2010, 12: 3356–3364
6 Jongsoo L J K. Approximate optimization of high-speed train nose shape for reducing micropressure wave. Industr Appl, 2008, 35: 79–87
7 Kwon H B, Jang K H, Kim Y S, et al. Nose shape optimization of high-speed train for minimization of tunnel sonic boom. Japan Soc Mech Eng, 2001, 4: 890–899
8 Ku Y C, Rho J H, Su H W, et al. Optimal cross-sectional area distribution of a high-speed train nose to minimize the tunnel micro-pressure wave. Struct Multid Optim, 2010, 42: 965–976
9 Lee S J, Kim B, Baik S W. Neural network modeling of inter-characteristics of silicon nitride film deposited by using a plasma-enhanced chemical vapor deposition. Expert Syst Appl, 2011, 38: 11437–11441
10 Kim B, Kwon M, Kwon S H. Modeling of plasma process data using a multi-parameterized generalized regression neural network. Microelectr Eng, 2009, 86: 63–67
11 Specht D F. A general regression neural network. IEEE T Neural Network, 1991, 2: 568–576
12 Leszek R. Generalized regression neural networks in time-varying environment. IEEE T Neural Network, 2004, 15: 576–596
13 Jamshid A S. Aerodynamic shape optimization based on free-form deformation. AIAA J, 2004. 2004–4630
14 Blazek J. Computational Fluid Dynamics Principles and Applications. New York: Elsevier Ltd., 2005. 16–17
15 Yan C. Method and Application of Computational Fluid Dynamics. Beijing: Beihang University Press, 2006. 236–237
16 Sobol I M, Shukman B V. Random and quasi-random sequences: Numerical estimates of uniformity of distribution. Math Comp Model, 1993, 18: 39–45
17 Donald R J. A taxonomy of global optimization methods based on response surfaces. J Global Optim, 2001, 21: 345–383